Modelling and Experimental Validation of a Loop Heat Pipe

M.C. Page[a], M.J. Brooks[b], L.W. Roberts[c], C. Bemont[d]

Received 25 March 2013, in revised form 30 May 2013 and accepted 13 September 2013

The Loop Heat Pipe (LHP) is a passive, two-phase heat transfer device employed in aerospace and, increasingly, terrestrial applications. A porous wick, placed solely in the evaporator, maintains circulation, and the remaining piping is a conduit for vapour and liquid. LHPs can transport heat over long distances, operate in adverse gravitational positions, tolerate numerous bends and are self-priming due to the compensation chamber passively providing liquid access to the wick. A robust mathematical model of the steady-state operation of an LHP for terrestrial high heat flux electronics was created and validated from data generated by an experimental LHP. The LHP was also operated in gravity-adverse and assisted elevations of 5° and 10°. The porous wick has a 60 % porosity, 6.77×10^{-13} m^2 permeability and an average pore radius of 1 µm. Ammonia was the chosen working fluid.The predicted values during the constant conductance mode of operation accurately reflected the experimental results. Theoretical values for the variable conductance mode were much less accurate and the model required additional empirical values to correct them. The maximum heat loads were 60 W, 50 W and 110 W for horizontal, gravity-adverse and gravity-assisted operation respectively.

Additional keywords: Sintered wick, two-phase modeling, gravity-assisted

Nomenclature

Roman

C_p	specific heat [J/kgK]
d	diameter [m]
dx	spatial increment [m]
f	frictional coefficient
G	thermal conductance [W/K]
h	coefficient of heat transfer [W/m^{2}K]
h_{fg}	latent heat of evaporation [J/kg]
k	thermal conductivity [W/mK]
K	permeability [m^2]
L	length [m]
$\dot{m}$	mass flow rate [kg/s]
M	mass [kg]
n	number of vapour grooves
P	pressure [Pa]
Q	heat [W]
r	radius [m]
r_{pore}	pore radius [m]
R	radius of curvature [m]
t	height of vapour grooves [m]
T	temperature [K]
(UA/L)	thermal conductance per unit length [W/mK]
v	velocity [m/s]
V	volume [m^3]
w	width of vapour groove [m]
X	vapour quality
Xtt	Lockhart-Martinelli parameter

Greek Symbols

α	void fraction
δ	film thickness [m]
Δ	incremental change
ε	porosity
μ	viscosity [Pa.s]
ρ	density [kg/m^3]
σ	surface tension [N/m]
τ	shear stress [N/m^2]
φ	angle of elevation [degrees]

Subscripts

amb	ambient
cap	capillary
cc	compensation chamber
cc-if	interface in compensation chamber
cc-wall	compensation chamber wall
ch	mass charge
eff	effective
ev	evaporator
ev-if	interface in evaporator
ev-wall	evaporator wall
f	fluid
fr	frictional
HL1	first heat leak
HL2	second heat leak
i	inner
in	CC inlet
l	liquid
ll	liquid line
mt	momentum transfer
o	outer

[a] Graduate Student, Mechanical Engineering, University of KwaZulu-Natal, Durban
Postal Address: P.O. Box 367, Amanzimtoti, 4125, South Africa
Email: 206505600@stu.ukzn.ac.za
[b] Senior Lecturer, Mechanical Engineering, University of KwaZulu-Natal, Durban
[c] Professor, Mechanical Engineering, University of KwaZulu-Natal, Durban
[d] Lecturer, Mechanical Engineering, University of KwaZulu-Natal, Durban

 © SAIMechE All rights reserved.

s	source
sad	saddle
v	vapour
vg	vapour grooves
vl	vapour lines
wall	transport line wall
wi	wick
wick	wick material

1. Introduction

Loop heat pipes (LHPs) are passive, two-phase heat transfer devices which use the capillary action of a porous wick in contact with a working fluid and a heat source to passively transport heat through evaporation and condensation mechanisms. A basic schematic of a LHP is shown in figure 1. It is composed of an evaporator, which houses the wick, a vapour line, condenser, liquid line and compensation chamber (CC). Heat from a source is transferred to the evaporator through a saddle. Liquid evaporates on the outer surface of the wick and the vapour collects in the vapour grooves. The vapour exits the evaporator and flows through the vapour line into the condenser where it condenses and subcools before flowing into the liquid line. The liquid finally exits into the CC. The CC has two purposes: 1) to allow a mass swing in the piping; and 2) to provide the wick with constant liquid contact. Liquid then enters the wick through its inner core and transitions outwards to replace the liquid being evaporated.

The use of a fine-pored wick isolated in the evaporator provides the LHP with certain advantages, such as the ability to transport heat over long distances, operate in adverse gravitational positions and to tolerate numerous bends in the transport lines. The LHP is also self-priming due to the CC passively providing the wick with constant liquid access.

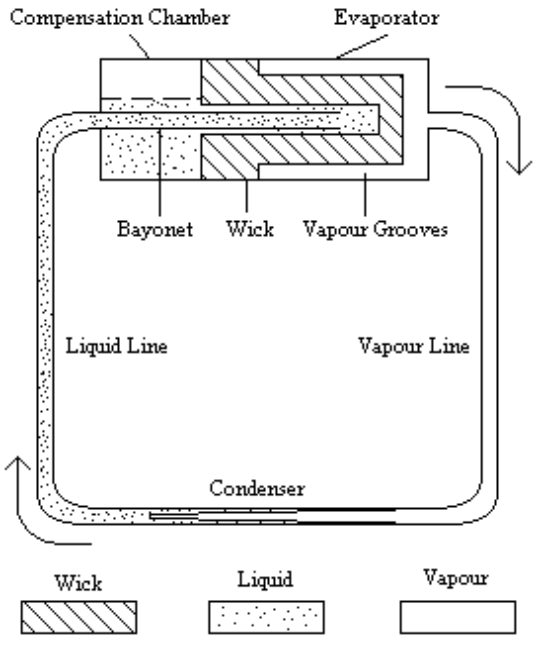


Figure 1: A schematic of a loop heat pipe

LHPs have been used in aerospace and aeronautical applications to fulfill thermal management requirements, such as operation in adverse gravity, which could not be satisfactorily performed by conventional heat pipes (Maydanik[1]). They are also considered superior to similar devices such as capillary pumped loops (CPL) which require preconditioning and can deprime (Ambirajan *et al.*[2]). In the interests of furthering the use of LHP devices for terrestrial applications, which is a growing area of interest (Pastukhov and Maydanik[3]), this research develops a theoretical model which can be used to simulate a single-wicked, terrestrial LHP and constructed an experimental LHP to validate the theoretical model and test the capabilities of the LHP.

2. Mathematical Heat Transfer Model

The model is divided into seven sections: 1) the evaporator and CC together, 2) the vapour grooves, 3) the vapour line, 4) the superheated portion of the condenser, 5) the two-phase portion of the condenser, 6) the subcooled portion of the condenser; and 7) the liquid line. While most of the mathematics has been developed from the work of Bai *et al.*[4], there are two significant differences in this model. Firstly, the evaporator and CC analysis partially reduces the need for empirical data.This was done to allow the model to be used as a generic design tool. Secondly, a void fraction correlation proposed by Wallis (Carey[5]) is utilized in the condenser model. The mathematical model is reproduced from an earlier conference paper by Page *et al.*[6].

2.1. Evaporator and compensation chamber

The evaporator and CC analysis uses a nodal network of temperatures and heat transfers, illustrated in figure 2.

Heat, Q_S, is transferred from the heat source, at a steady-state temperature of T_S, through the saddle to the outer wall of the evaporator. Fourier's Law of Thermal Conduction is used to calculate the saddle thermal conductance, G_{sad}.

$$Q_s = G_{sad}(T_s - T_{ev-wall}) \quad (1)$$

Q_s is split, with the majority of the heat transferred to the liquid/vapour interface on the outer surface of the wick while the remainder is leaked between the evaporator and CC walls. The thermal conductance along this latter path, G_{HL1}, is found using Fourier's Law through the envelope between them. Bai *et al.*[4] suggest a length equal to the wick length added to half the length of the CC. The general equation for the heat leak is then:

$$Q_{HL1} = G_{HL1}(T_{ev-wall} - T_{cc-wall}) \quad (2)$$

Equation (2) requires the temperature of the CC wall. This temperature cannot be determined from available data and is assumed as an input.

The general relation for the heat transferred to the liquid-vapour interface, $Q_{ev\text{-}if}$, is:

$$Q_{ev-if} = G_{ev}(T_{ev-wall} - T_{ev-if}) \quad (3)$$

 © SAIMechE All rights reserved.

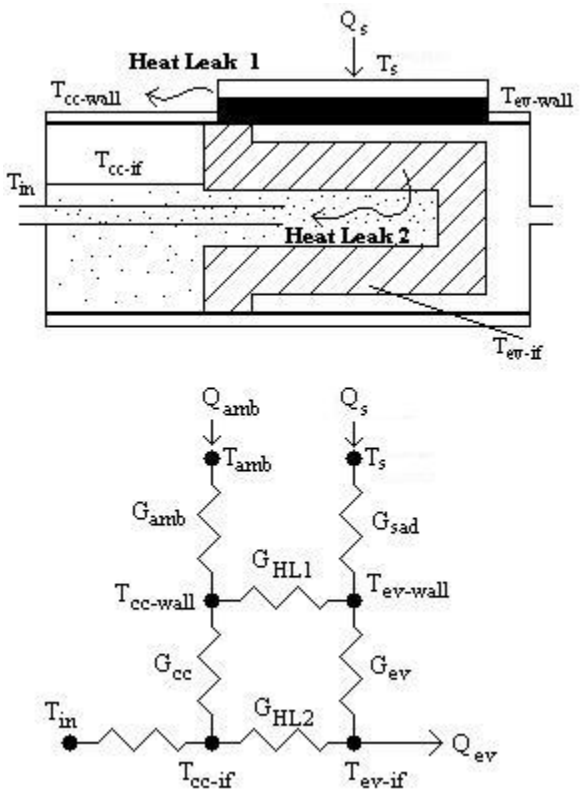


Figure 2: Evaporator and compensation chamber nodal network

G_{ev} is influenced by factors such as the nature of the thermal contact between the wick and evaporator wall and the geometry of the wick. It is also influenced by additional vapour related phenomena, such as the liquid-vapour interface retracting deeper into the pores and localised dry spots where the wick contacts the evaporator wall (Chernyshev and Maydanik[7]). Measurements of the evaporator wall and vapour line inlet temperatures are required to calculate it in lieu of an accurate analytical calculation (Vlassov and Riehl[8]). In this study, G_{ev} was considered to only vary slightly with heat load as the conductivity and structure of the wick are constant and the effects of vapour phenomena are neglected. The conductance is found as an average and applied for all heat loads. This is the first reduction in empirical reliance.

There is another division of heat at the liquid-vapour interface. The interface and the fluid in the CC are thermally coupled, resulting in a second heat leak.

$$Q_{HL2} = G_{HL2}\left(T_{ev-if} - T_{cc-if}\right) \tag{4}$$

Heat is transferred through the wick from the outer surface to the wick core through the metallic structure of the wick and liquid in the pores. Some heat is also used, in parallel with the previous heat transfer, to raise the temperature of the liquid transitioning through the wick. The heat leak is then transmitted from the wick core to the two-phase interface in the CC through an evaporation/condensation mechanism. To determine the thermal conductance of the wick, Bai *et al.*[4] use the Navier-Stokes energy equation to analyse the temperature distribution through the wick in a purely radial direction, producing the following equation:

$$Q_{wi} = \frac{\dot{m}C_{pl}}{\left(\frac{d_o}{d_i}\right)^{\eta} - 1}\left(T_{ev-if} - T_{cc-if}\right) \tag{5}$$

where the exponent η is given as:

$$\eta = \frac{\dot{m}C_{pl}}{2\pi k_{eff} L_{wi}} \tag{6}$$

The equation proposed by Chaudary and Bhandari (Bai *et al.*[4]) is used to determine the effective thermal conductivity.

$$k_{eff} = (k_{max})^n \times (k_{min})^{1-n} \tag{7}$$

The exponent n in equation (7) can vary between 0.42 and 0.5, Bai *et al.*[4] suggesting a value of 0.42. The two values k_{max} and k_{min} refer to the parallel and serial thermal conduction paths respectively. They are determined by the following equations:

$$k_{max} = \varepsilon \times k_f + (1-\varepsilon) \times k_{wick} \tag{8}$$

$$k_{min} = \frac{k_f k_{wick}}{\varepsilon k_{wick} + (1-\varepsilon) \times k_f} \tag{9}$$

The heat used to raise the temperature of the liquid is given as:

$$Q_f = \dot{m}C_{pl}\left(T_{ev-if} - T_{cc-if}\right) \tag{10}$$

The two-phase heat transfer in the saturated CC fluid is difficult to determine and involves the use of advanced modeling software (Chernysheva and Maydanik[9]). However, with the use of a bayonet to flood the wick core, the two-phase heat transfer is considered negligible in this model. The second heat leak is given by the summation of equations (5) and (10).

The remainder of $Q_{ev\text{-}if}$ is used to boil the liquid on the surface of the wick, expressed as:

$$Q_{ev} = \dot{m}h_{fg} \tag{11}$$

The calculations for Q_{HL2} and Q_{ev} are interdependent and require additional information. The model requires two assumed values as inputs: the second heat leak and the CC temperature.

In the CC, heat is transferred between the CC wall and the ambient environment, given as:

$$Q_{amb} = G_{amb}(T_{amb} - T_{cc-wall}) \tag{12}$$

Since this model is of a terrestrial LHP in an open environment, the heat transfer mechanism is natural convection and the conductance coefficient G_{amb} is expressed as:

$$G_{amb} = 1.32\pi L_{cc} d_o \left(\frac{T_{cc-wall} - T_{amb}}{d_o}\right)^{0.25} \tag{13}$$

At the CC wall, Q_{HL1} is added to Q_{amb} and the resulting heat is transferred to the fluid in the CC. The heat transfer between the CC wall and CC fluid is given as:

$$Q_{cc} = G_{cc}\left(T_{cc-wall} - T_{cc-if}\right) \tag{14}$$

This thermal conductance is dependent on factors such as the movement of the fluid in the CC and the CC void fraction which makes it difficult to determine analytically. G_{CC} is usually found empirically using the temperatures of the fluid at the CC inlet, CC wall, evaporator wall and vapour line inlet (Vlassov and Riehl[8]). Unlike the empirical determination of G_{ev}, the estimation of G_{CC} would have to be generated for every scenario of operation. G_{CC} is not required, however, as the temperature of the CC fluid interface is already assumed from the calculation of the second heat leak. This is the second reduction in empirical reliance.

For steady-state operation, the heat from the CC wall and second heat leak through the wick are combined to heat the subcooled liquid from the CC inlet. The general equation for the heating of the subcooled liquid is given as:

$$Q_{in} = \dot{m}C_{pl}\left(T_{cc-if} - T_{in}\right) \tag{15}$$

Equation (15) requires that the inlet temperature be assumed to determine the heat capacity of the liquid. By assuming this temperature, the heat required to raise the temperature of the subcooled inlet liquid to the temperature of the CC fluid interface can be calculated and compared to the value of the sum of Q_{CC} and the second heat leak. This energy balance is used in the model solution.

The assumed temperatures of the CC wall, CC fluid and CC inlet are constrained by upper and lower limits. These limits are expressed as:

$$T_{ev-wall} > T_{cc-wall} > T_{cc-if} > T_{in} > T_{cond} \tag{16}$$

2.2. Vapour grooves

Due to continuing evaporation along the grooves, the low conductivity of the vapour and its quick passage through the grooves, the vapour temperature remains constant. However, due to a drop in pressure through the grooves, the vapour superheats. At high heat loads, it is possible for the vapour temperature to increase beyond its saturation temperature but this is neglected for the sake of generality.

Bai *et al.*[4] assume the flow rate increases linearly along the length of the grooves. This allows the maximum mass flow rate to be assumed for half the length of the vapour grooves and the pressure drop, adjusted with the hydraulic diameter of the grooves, is calculated in a single step:

$$\Delta P_{vg} = -f\frac{L_{vg}(t+w)\dot{m}^2}{4n^2t^3w^3\rho_v} \tag{17}$$

The coefficient of friction, f, is calculated from the Poiseuille and Blasius correlations. For Moody frictional coefficients, these are:

$$f = \frac{64}{\mathrm{Re}} \text{ for } \mathrm{Re} < 2200 \text{ (Laminar Flow)} \tag{18}$$

$$f = 0.3164\mathrm{Re}^{-0.25} \text{ for } \mathrm{Re} > 2200 \text{ (Turbulent Flow)} \tag{19}$$

where the Reynolds number, Re, is given by:

$$\mathrm{Re} = \frac{\rho v d}{\mu} = \frac{2\dot{m}}{(t+w)\mu_v} \tag{20}$$

2.3. Vapour and liquid lines

The change in temperature and pressure defined here apply to both transport lines and are adapted from the model of Bai *et al.*[4]. The temperature change of the fluid is due to thermal contact with the surrounding terrestrial atmosphere. The general equation for the temperature change, assuming that heat is rejected from the fluid, is:

$$\frac{dT_f}{dx} = -\frac{1}{\dot{m}C_p}\left(\frac{UA}{L}\right)\left(T_f - T_{amb}\right) \tag{21}$$

where the thermal resistance is given by the sum of the resistances between them:

$$\frac{L}{UA} = \frac{1}{h_i d_i \pi} + \frac{\ln(d_o/d_i)}{2\pi k_{wall}} + \frac{1}{h_o d_o \pi} \tag{22}$$

The fluid has a convective thermal resistance characterised by the coefficient of heat transfer, h_i:

$$h_i = \frac{(\mathrm{Nu})k_f}{d_i} \tag{23}$$

The fluid is considered to be fully developed and steady. The fully-developed consideration is due to the high length to diameter ratio of the tubing. The Nusselt number can be found using the Reynolds number calculated using equation (20). For laminar flow:

$$\mathrm{Nu} = 4.36 \text{ for constant heat flux} \tag{24}$$

$$\mathrm{Nu} = 3.66 \text{ for constant temperature} \tag{25}$$

For turbulent flow, the Nusselt number is given by the Dittus-Boelter correlation:

$$\mathrm{Nu} = 0.023\mathrm{Re}^{0.8}\mathrm{Pr}^{\mathrm{n}} \tag{26}$$

where the exponent, n, is 0.4 when the fluid is being heated and 0.3 when the fluid is being cooled. The Prandtl number, Pr, is found using the following equation.

$$\mathrm{Pr} = \frac{C_p\mu}{k} \tag{27}$$

 © SAIMechE All rights reserved.

The thermal resistance of the wall is given by Fourier's Law through a cylinder. The coefficient of heat transfer provided by natural convection on the outside of the pipe is expressed as:

$$h_o = 1.32\left(\frac{T_o - T_{amb}}{d_o}\right)^{0.25} \tag{28}$$

The pressure drop in the transport lines due to both friction and gravity is given as:

$$\frac{dP_f}{dx} = -f\frac{8\dot{m}^2}{\rho_f \pi^2 {d_i}^5} \pm g\rho_f \sin\varphi \tag{29}$$

The frictional coefficient is found using Eqs. (18-20). The gravitational pressure change develops when the condenser is elevated or lowered relative to the evaporator. A positive angle φ is used when the condenser is elevated above the evaporator and the flow is gravitationally assisted. Equation (29) is altered to reflect gravity for each line: the sign before the gravitational term is positive for the liquid line and negative for the vapour line.

The model calculates the temperature and pressure of the fluid by dividing the transport lines into discrete increments, *dx*, and determining the change in these qualities per increment over the length of the transport lines.

2.4. Condenser

The condenser is separated into the superheated region, the two-phase region and the subcooled region. The superheated and subcooled regions are modelled using the same equations as the transport lines but with a different heat sink temperature and resistance. The two-phase region requires its own numerical model.

The two-phase region assumes an annular flow regime, where the condensing liquid phase accumulates on the walls of the tubing while the pure vapour phase remains in the central stream. This is reasonable because the mass flow rate is relatively low and annular phase distributions are commonly made when analysing small-to-capillary diameter pipe flow. The analysis of the two-phase region is adapted from the Bai *et al.*[4] model and required four variables and their change over an increment *dx* to be determined: the vapour quality, *X*; the film thickness, δ; the vapour pressure, P_v; and the liquid pressure, P_l.

The vapour quality is the ratio of the vapour mass over the total mass. Its change as a result of condensation is given as:

$$\frac{dX}{dx} = -\frac{1}{\dot{m}h_{fg}}\left(\frac{UA}{L}\right)(T_v - T_{heat\ sink}) \tag{30}$$

The thermal resistance is given by equation (22), altered to reflect the nature of the heat exchanger. The first convective term is the thermal resistance offered by the liquid film. Its coefficient of heat transfer can be found using equation (23). The hydraulic diameter of the liquid film required for this calculation is given by:

$$d_i = 4\delta - \frac{2\delta^2}{r_i} \tag{31}$$

The change in film thickness is found by analysis of the curvature of the interface between the vapour and liquid regions, given by the Young-Laplace equation:

$$P_v - P_l = \sigma\left(\frac{1}{R_{radial}} + \frac{1}{R_{axial}}\right) \tag{32}$$

The R_{radial} and R_{axial} terms are the radii of curvature in the radial and axial directions respectively. The axial radius of curvature tends towards infinity as the overall change in film thickness in the axial direction is small and occurs over a large distance. The radial curvature can be expressed as a function of the film thickness and the contact angle between the phases. The pressure difference as a result of change in film thickness is:

$$P_v - P_l = \frac{\sigma}{r_i - \delta}\left(1 + \left(\frac{d\delta}{dx}\right)^2\right)^{-0.5} \tag{33}$$

The vapour pressure decreases due to three factors: a frictional shear stress; a change in momentum; and a momentum transfer shear stress. The latter stress is introduced by Bai *et al.*[4]. The general equation for the pressure drop in the vapour region is given as:

$$\frac{dP_v}{dx} = -\frac{2}{r_i - \delta}(\tau_{fr} + \tau_{mt}) - \frac{d(\rho_v {v_v}^2)}{dx} \tag{34}$$

The frictional shear stress develops at the interface of the two phases because the vapour and liquid travel at different velocities. The liquid has laminar flow for most of the condenser length and as such the velocity at the interface can be considered to be twice the average velocity. The frictional shear stress is given by:

$$\tau_{fr} = \pm\frac{1}{8} f\rho_v (v_v - 2v_l)^2 \tag{35}$$

where both velocities are calculated as the average velocity of the phase. The variable sign at the beginning of the equation should be negative when the liquid velocity is larger than the vapour velocity. The coefficient of friction is calculated using Eqs. (18-20). The momentum-transfer shear stress is also dependent on the difference between vapour and liquid velocities and takes condensation into account. It is given as:

$$\tau_{mt} = -\frac{dX}{dx}\frac{X\dot{m}}{2\pi(r_i - \delta)}(v_v - 2v_l) \tag{36}$$

Finally, the momentum term describes the force acting on the vapour as its momentum changes through condensation.

An empirical void fraction correlation proposed by Wallis (Carey[5]) is the completing equation and allows the

 © SAIMechE All rights reserved.

film thickness to be determined from the pressures and quality at a cross section. It is given as:

$$\alpha = \frac{V_v}{V_{total}} = (1 + Xtt^{0.8})^{-0.378} \quad (37)$$

where *Xtt*, the Lockhart-Martinelli parameter, is given by:

$$Xtt = \left(\frac{1-X}{X}\right)^{0.9} \left(\frac{\rho_v}{\rho_l}\right)^{0.5} \left(\frac{\mu_l}{\mu_v}\right)^{0.1} \quad (38)$$

With the key values known at the beginning of any spatial increment, their outlet values can be found. The outlet vapour quality and vapour pressure can be calculated directly from the entry values of the increment while the liquid pressure and film thickness solution requires a corrective loop. First, assuming the liquid pressure equals the vapour pressure, the outlet film thickness is calculated using the void fraction correlation. This then gives the change in the film thickness over *dx*. Using equation (33) and these values, the correct liquid pressure can be calculated. This value is then substituted for the assumed liquid pressure and the process repeated until there is no change in liquid pressure and film thickness between iterations.

2.5. Mass equation

The model requires that the fluid mass and void fraction in the CC be known. The former is given as:

$$M_{cc} = M_{ch} - M_{wi} - M_{vg} - M_{vl} - M_{cond} - M_{ll} \quad (39)$$

and the latter as:

$$\alpha = \frac{\rho_l V_{cc} - M_{cc}}{(\rho_l - \rho_v) V_{cc}} \quad (40)$$

A void fraction exists in the CC during the variable mode of operation, typically under low heat loads. As the heat load increases, the void fraction decreases to zero and the CC floods. Due to the CC no longer being able to store excess fluid, there is a steady reduction in the length of the two-phase region of the condenser as the heat load increases. The LHP is then in constant conductance mode as the restriction on the two-phase length necessitates greater operational temperatures.

2.6. Model solution

The model is implemented in MATLAB and determines the correct temperature of the heat source, T_s, for a given heat load, Q_s. This temperature fulfils three criteria: an energy balance must exist in the CC; the void fraction in the CC must be acceptable; and the pressure drop in the system cannot be larger than the maximum capillary head which the wick can produce.

The four initial assumed values are first corrected. These are: the second heat leak, Q_{HL2}; the temperature of the CC wall, $T_{cc\text{-}wall}$; the temperature of the CC fluid, $T_{cc\text{-}if}$; and the temperature of the CC inlet, T_{in}. The second heat leak can be corrected for an assumed CC wall and CC fluid temperature over a number of iterations with equation (4), (5), (10) and (11). Calculating the temperatures and pressures throughout the outer loop outputs the liquid line outlet temperature, which is the correct value of T_{in}. The pressure at the liquid line outlet determines a corresponding saturation temperature, which is the correct value of $T_{cc\text{-}if}$.

To reduce the dependency on experimental data, the model is configured such that G_{cc} is not needed. The model does not explicitly determine the CC wall temperature, and it remains an assumed value. Instead, the model algorithm generates two sets of operating temperatures for a given heat load: one set in which the assumed $T_{cc\text{-}wall}$ value is slightly below $T_{ev\text{-}wall}$; and a second set in which $T_{cc\text{-}wall}$ is slightly greater than $T_{cc\text{-}if}$.

The model determines whether the source temperature produces the requisite energy balance in the CC once the assumed values have been corrected. If not, the source temperature is changed and the process repeated.

The model then analyses whether equation (40) produces a void fraction between the maximum permissible value and zero. A maximum permissible void fraction of 0.5 guarantees liquid/wick contact (Riehl[10]). If it does, the CC contains a void and the void fraction is acceptable.

If the void fraction is less than 0, the CC has become flooded and the LHP has entered its constant conductance mode of operation. The CC fluid is subcooled to a temperature between the saturated CC fluid and CC inlet temperatures. This temperature cannot be calculated explicitly and is incrementally decreased until an energy balance and a void fraction of zero are established. If neither occurs before the CC fluid temperature equals the CC inlet temperature, the source temperature is changed and the process repeated.

The final criterion is whether the system pressure drop is less than the maximum capillary head. The following summation of the pressure drops in each component is used:

$$\Delta P_{system} = \Delta P_{wi} + \Delta P_{vg} + \Delta P_{vl} + \Delta P_{cond} + \Delta P_{ll} \quad (41)$$

The pressure drop through the wick is provided by Darcy's Law:

$$\Delta P_{wi} = \frac{\dot{m}\mu_l \ln\left(\frac{d_o}{d_i}\right)}{2\pi\rho_l K_{wi} L_{wi}} \quad (42)$$

The capillary action varies to maintain circulation but has a maximum value associated with the pore radius. The maximum capillary head is given as:

$$\Delta P_{cap} = \frac{2\sigma}{r_{pore}} \quad (43)$$

Once all three criteria are met and the steady-state temperature profile is recorded, the CC wall temperature is changed and the other profile generated.

 © SAIMechE All rights reserved.

3. Experimental LHP

The specifications of the experimental LHP are given in table 1. A 400 W plate heater and a coaxial water jacket with countercurrent flow, ice cooled to approximately 8°C, were employed. 9 T-type thermocouples were installed and the layout of the instrumentation is given in figure 3. The maximum instrumentation error is approximately 3°C. The source temperature was taken as the larger reading of either T1 or T2. The working fluid was ammonia due to its high latent heat of evaporation and large saturated pressure difference across a small temperature difference. The physical LHP is shown in figure 4.

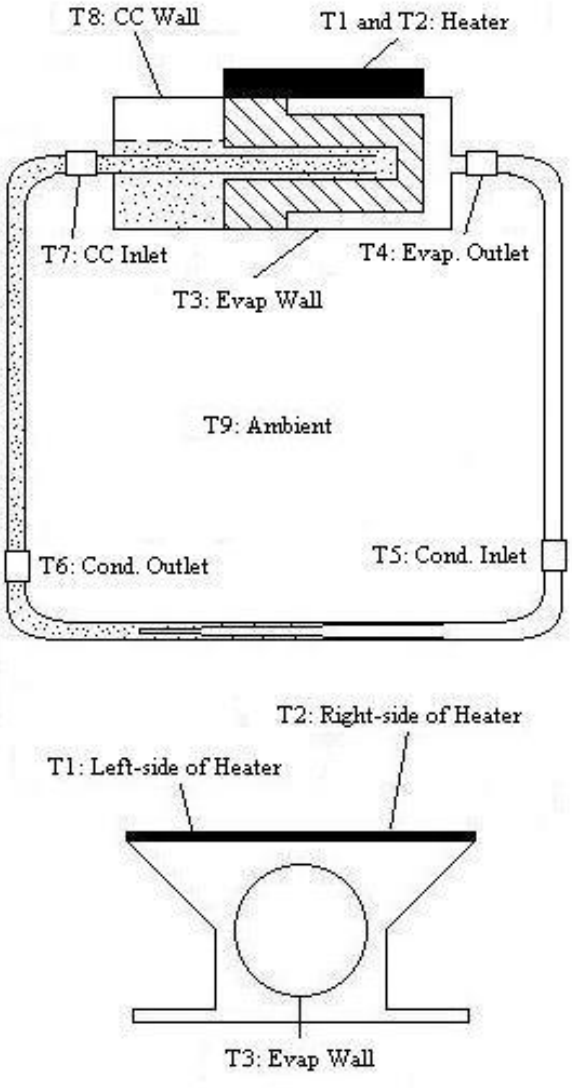


Figure 3: Distribution of thermocouples throughout LHP

The porous wick had to be sintered with satisfactory properties. A study was performed with the intention of optimising sintering temperature to produce a wick with ideal porosity, permeability and pore radius for a lead up and dwell time of 2.5 hours and 10 minutes respectively.

The wick was manufactured from nickel powder primarily for its corrosion resistance and the nickel powder had an average particle diameter of 10 µm. Porosity was found using a density test while the permeability was found using the Carmen-Kozeny equation (Xin *et al.*[11]):

$$K = \frac{d^2\varepsilon^3}{180(1-\varepsilon)^2} \tag{44}$$

where d is the average particle diameter. Figure 5 shows the results for porosity and permeability.

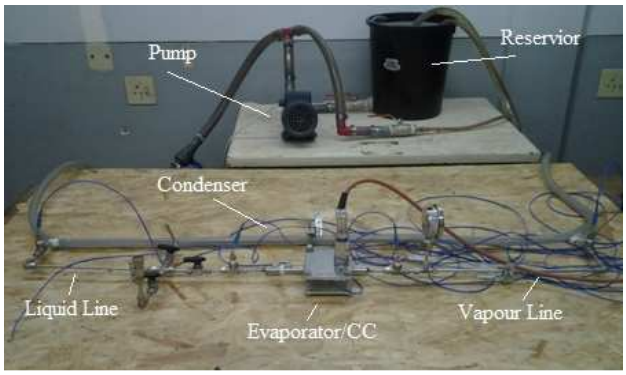


Figure 4: Layout of LHP

Table 1. LHP specifications

Saddle	Length	100 mm
	Width	130 mm
	Thickness	30 mm
	Material	Aluminum
Evaporator	Length	100 mm
	OD/ID	20 mm /16.5 mm
	Envelope Material	Stainless Steel 316
CC	Length	60 mm
	OD/ID	20 mm/16.5 mm
	Envelope Material	Stainless Steel 316
Vapour Line	Standard Length	0.64 m
	OD/ID	6.4 mm/3 mm
	Envelope Material	Stainless Steel 316
Liquid Line	Standard Length	0.655 m
	OD/ID	6.4 mm/3 mm
	Envelope Material	Stainless Steel 316
Condenser	Length	1.25 m
	OD/ID	6.4 mm/3 mm
	Envelope Material	Stainless Steel 316
Bayonet	Length	110 mm
	OD/ID	4 mm/3 mm
	Envelope Material	Stainless Steel 316
Working Fluid	Fluid	Ammonia
	Mass Charge	~0.021 kg

Average pore radius was found by statistical analysis of scanning electron microscope (SEM) images of wick cross sections. One such image is shown in figure 6. The pore sizes are calculated by analysis of binary maps which define the shape and number of pores. No correlation was found between the pore radius and sintering temperature and the pore radii were found to vary between 0.56 µm and 0.64 µm. A pore size of 1 µm was used instead which introduces a safety factor. The specifications of the machined wick installed into the LHP are given in table 2 and the final wick can be seen in figure 7.

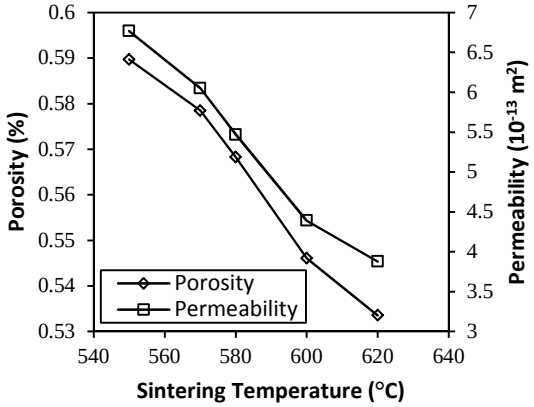


Figure 5: Porosity and permeability versus sintering temperature

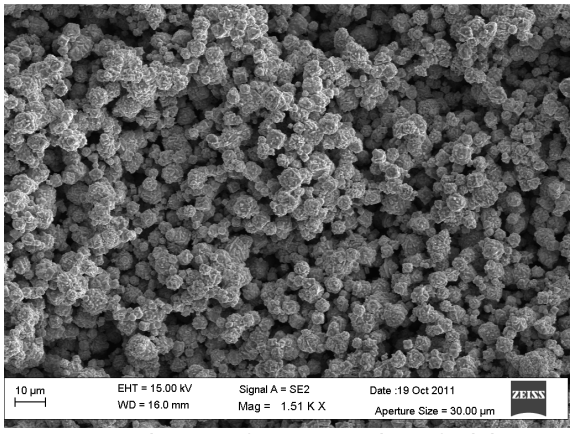


Figure 6: SEM image of cross section of wick magnified 1500 times

Table 2.Specifications of porous sintered wick

Wick	Material	Nickel
	Porosity	~60%
	Permeability	6.77x10^{-13} m^2
	Pore radius	1 µm
	Length	80 mm
	OD	16.5 mm
	ID	7 mm
Vapour Grooves		
Longitudinal	Length	50 mm
	Height/width	2 mm/ 2 mm
	Number	6
Azimuthral	Height/width	2 mm/2mm
	Number	3



Figure 7: Sintered porous wick with machined vapour grooves and inner cavity

4. Results

The steady-state temperature profile is shown in figure 8. The maximum system pressure was limited to 18 bar for safety reasons, preventing operation at larger heat loads. Despite its low heat load, the LHP had a promising overall thermal resistance, as shown in figure 9. The overall thermal resistance is given as:

$$R_{overall} = \frac{(T_s - T_{heat\ sink})}{Q_s} \tag{45}$$

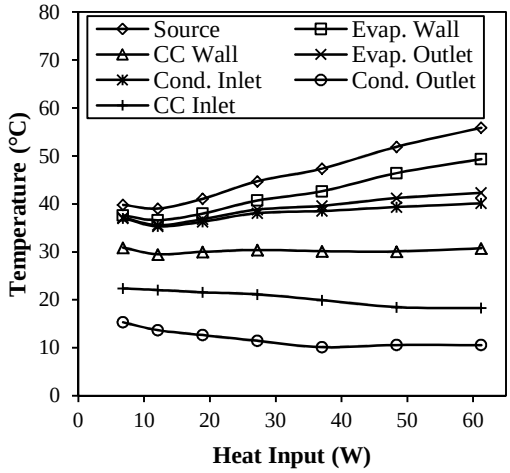


Figure 8: Temperature profile for LHP under steady-state conditions

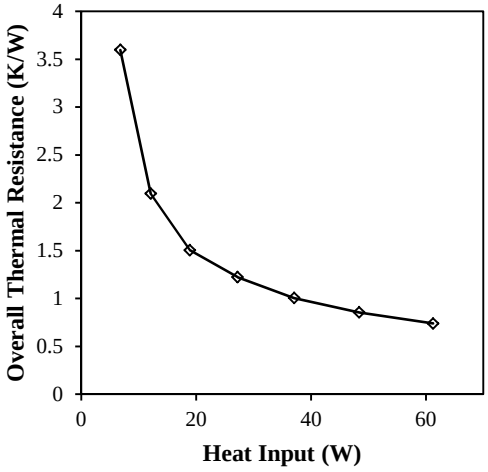


Figure 9: Overall thermal resistance of LHP

 © SAIMechE All rights reserved.

Despite its aim to reduce dependence on experimental data, the mathematical model required a number of heat load dependent empirical adjustments, given in table 3. The constant thermal conductance of the evaporator, G_{ev}, was found to vary and an average of 9.13 W/K was used in accordance with the aim of reducing empirical dependence. To examine the impact of this, the temperature profile of an empirically accurate model, with experimental G_{ev} values and additional vapour superheating, was compared to that of a model containing only the averaged G_{ev} value. It was found that they had good agreement, with the source temperature differing by approximately 3° degrees. The model was also not able to perfectly determine the mass in the CC and the mass charge was given a tolerance of 1%.

Table 3: Experimental amendments to model

Heat Load (W)	7	12	19	27	37	48	61
$T_{heat\ sink}$ (°C)	15	13	12	11	10	10	10
Factor by which h_0 is adjusted for liquid line	0.5	0.5	0.5	0.4	0.4	0.3	0.3
G_{sad} (W/K)	3.1	4.9	6.1	6.8	7.9	8.8	9.4

The variable conductance mode of operation was found to be highly inaccurate, with theoretical temperatures being up to 16°C lower than the experimental values. This was due to the model not taking into account the two-phase heat transfer between the interfaces in the evaporator and CC. The heat leak could be empirically determined using the temperatures of the evaporator wall and outlet and the CC wall and inlet. Values of 0.46 W and 0.66 W for 7 W and 12 W heat loads respectively were found and included in the modeling of the variable conductance mode. The thermal conductance between the CC fluid and CC wall, G_{CC}, could also be empirically determined and was used to correct the CC wall temperature assumption. These were 0.0095 W/K and 0.0025 W/K for 7 W and 12 W respectively.

With these amendments, the model generated temperature profiles for both CC temperature scenarios. These are compared with experimental results in figure 10. Note that the evaporator outlet and condenser inlet temperatures are approximately equal because condensation occurs early in the vapour line and thus both curves are expressed with the evaporator outlet curve. The two CC wall temperature curves are not included for clarity of the graph but they would be approximately equal to either the evaporator wall or CC fluid temperature curves. The condenser outlet and CC inlet were approximately equal for both the maximum and minimum operating temperatures and only a single curve for each is shown.

The model was reasonably accurate during both the variable conductance mode and constant conductance mode once the required empirical adjustments were made. Although the low temperature curves appear to be highly accurate, the high temperature curve should be considered as a safety factor if the model is refined into a design tool. The use of a heat load independent value of G_{ev} and upper and lower temperature profiles were shown to produce acceptably accurate theoretical values.

Gravity influenced operation was conducted by elevating either the evaporator over the condenser (gravity-adverse) or with the condenser over the evaporator (gravity-assisted). The LHP was tested at 5° and 10° gravity-adverse and gravity-assisting elevations. The source temperature curves for these scenarios and horizontal operation are compared in figure 11. The LHP operated successfully when adversely elevated but with lower acceptable heat loads. Gravity-assisted elevation showed much better performance, allowing a maximum heat load of 109 W to be dissipated at 10°.

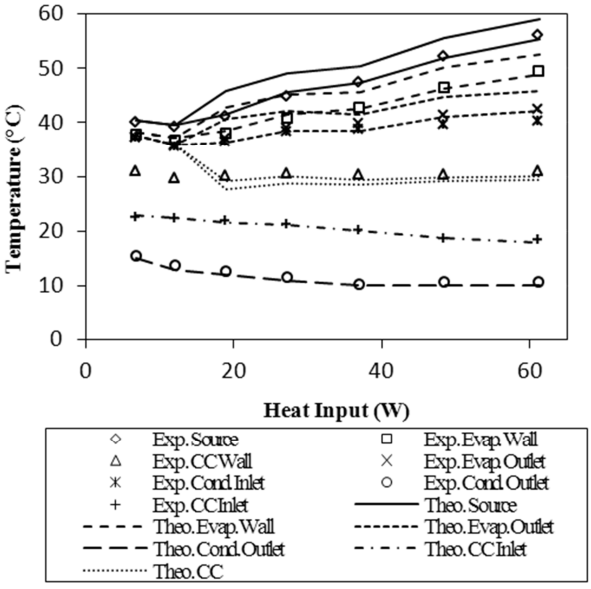


Figure 10: Comparison of theoretical and experimental temperature profiles of LHP

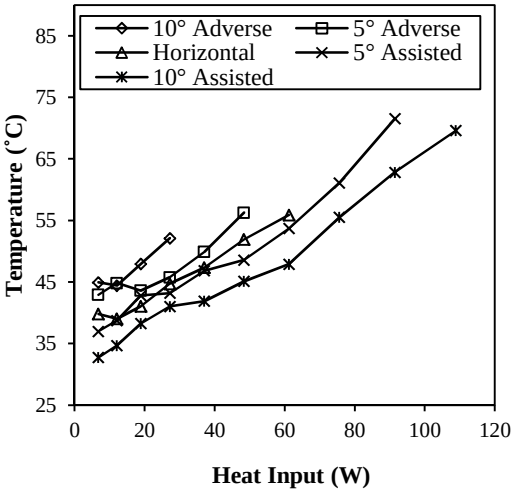


Figure 11: Source temperature curves for gravity-adverse and -assisted elevations of the LHP

5. Conclusion

The mathematical model detailed here was designed to simulate a single-wicked, terrestrial LHP under steady-

state conditions. To reduce reliance on empirical data, the model assumes a heat load independent evaporator thermal conductance and uses a varying CC wall temperature to bypass the need to determine the CC thermal conductance. However, the model still requires certain adjustments which prevent it being used as a generic design tool. The simulated results are accurate during the constant conductance mode of operation but accuracy is reduced during the variable conductance mode due to the neglect of two-phase heat transfer in the second heat leak. Additional empirical data is required to correct for this. The LHP itself operated as expected although its maximum heat load was only 61 W. Gravity influenced operation demonstrated that the LHP could operate in adverse gravity but with lower heat loads and higher operating temperatures. Gravity-assisted operation was highly successful, allowing 109 W to be dissipated at an elevation of 10°.

Acknowledgements

This research was supported and funded by the National Research Foundation of South Africa and the Eskom TESP Programme.

References

1. Maydanik YF, Loop heat pipes, *Applied Thermal Engineering*, 2005, 25(5), 635–657.
2. Ambirajan A, Adoni AA, Vaidya JS, Rajendran AA, Kumar D, Dutta P, Loop heat pipes: A review of fundamentals, operation and design, *Heat Transfer Engineering*, 2012, 33(4-5): 387-405.
3. Pastukhov VG, Maydanik YF, Low-noise cooling system for PC on the base of loop heat pipes, *Applied Thermal Engineering*, 2007, 27(5), 894-901
4. Bai L, Lin G, Zhang H, Wen D, Mathematical modeling of steady-state operation of a loop heat pipe, *Applied Thermal Engineering*, 2009, 29(13), 2643–2654.
5. Carey VP, *Liquid-Vapor Phase Change Phenomena: An Introduction to the Thermophysics of Vaporization and Condensation Processes in Heat Transfer Equipment*, Hemisphere, Washington, 1992.
6. Page MC, Brooks MJ, Bemont C, Roberts LW, Progress on performance validation of a steady-state loop heat pipe model, *AIAA 10th Annual International Energy Conversion Engineering Conference*, Atlanta, Georgia, USA, 29 July – 1 August 2012.
7. Chernysheva MA, Maydanik YF, 3D-model for heat and mass transfer simulation in flat evaporator of copper-water loop heat pipe, *Applied Thermal Engineering*, 2012, 33, 124-134.
8. Vlassov VV, Riehl RR, Mathematical model of a loop heat pipe with cylindrical evaporator and integrated reservoir, *Applied Thermal Engineering*, 2008, 28(8), 942-954.
9. Chernysheva MA, Maydanik YF, Numerical simulation of transient heat and mass transfer in a cylindrical evaporator of a loop heat pipe, *International Journal of Heat and Mass Transfer*, 2008, 51(17), 4204-4215.
10. Riehl RR, Extensive development of the loop heat pipe technology, *Proceedings of 36th International Conference on Environmental Systems*, Norfolk, Virginia,USA, 17 July 2006.
11. Xin G, Cui K, Zou Y, Cheng L, Development of sintered Ni-Cu wicks for loop heat pipes, *Science in China Series E: Technological Sciences*, 2009, 52(6), 1607-1612.

 © SAIMechE All rights reserved.